ROYAL SOCIETY
OF CHEMISTRY

PAPER

Check for updates

Modulating hardness in $Sc_2(Ru_{5-x}TM_x)B_4$ through empirical considerations and computational analysis†

Jacob C. Hickey [ID] [ab] and Jakoah Brgoch*[ab]

Ternary and higher-order borides remain an underexplored area in the search for hard materials. The difficulties associated with purely systematic experimental investigations have largely hindered the consideration of such complex phases. Here, traditional design rules are merged with computation-based methods to direct synthetic efforts, addressing this challenge. The compound $Sc_2Ru_5B_4$ was selected to demonstrate this approach. The phase was first prepared using arc melting, and the crystal structure was resolved with single-crystal X-ray diffraction. Vickers microhardness indentation revealed that $Sc_2Ru_5B_4$ is a hard metal, and the mechanical properties can be enhanced by substituting Ru for the isoelectronic but more electron-dense Os following an empirical understanding of hardness in borides. Analyzing the ensuing density of states (DOS) of $Sc_2(Ru_4Os)B_4$ indicates the Fermi level nevertheless falls in an unfavorable position requiring a reduction in the electron count to optimize the electronic structure. The subsequent synthesis of $Sc_2(Ru_4TM)B_4$ (TM = Ta, W, Re, and Ir) alters the electron count moving the Fermi level from the peak. At the same time, Vickers indentation measurements, combined with DFT-level stress–strain calculations and a bonding analysis, show that shifting the Fermi level reduces the occupation of antibonding interactions, which also increases the hardness. These data suggest that electron density, Fermi level position, and chemical bonding are essential markers when developing high hardness materials.

Introduction

Transition metal borides are an intriguing class of structural materials due to their exceptional mechanical properties, including high hardness, high bulk modulus, and high shear modulus.[1,2] Hard metal borides are found in various tools and abrasives like drill bits or sandpaper, and they are essential to the aerospace and military industries. The resulting extensive research on binary metal borides like TiB_2,[3,4] ZrB_2,[5] ReB_2,[6,7] and WB_4[8] for these applications has all but eliminated discoveries in the binary phase space.[9,10] Thus, a transition to the underexplored ternary and higher-order boride systems may prove beneficial to advance the development of high hardness materials.[11]

There are multiple routes for discovering complex, high hardness borides. Exploratory materials synthesis is among

the most common, where known compounds are selected from crystal structure repositories, like the Inorganic Crystal Structure Database (ICSD), based on reported design criteria. This generally includes combining transition metals with high valence electron density with short, covalent bond forming elements.[2,12] The compounds are then prepared using high-temperature synthetic approaches and characterized with Vickers microhardness (H_V) indentation measurements. Many new high hardness materials have been reported using this valuable, albeit time-consuming, approach.[9] Materials with an already known hardness can also be improved through solid solution hardening, work hardening, and grain-boundary optimization.[13–15] For example, incorporating $\approx 50\%$ W in ReB_2 yields a $\approx 16\%$ increase in H_V.[16] Multicomponent alloys, sometimes termed high entropy alloys (HEA), containing five or more elements are an extreme version of solid solutions that have similarly gained attention due to their remarkable mechanical properties.[17–19] For instance, five-component metal diborides prepared in the AlB_2-type structure have been shown to possess impressive hardness and oxidation resistance that is generally better than their binary components.[17] Sintering the boron-doped HEA $(VNbMoTaW)_{99}B_1$ at various temperatures has also shown the ability to modulate the grain size and

ᵃ Department of Chemistry, University of Houston, Houston, Texas 77204, USA. E-mail: jbrgoch@uh.edu

ᵇ Texas Center for Superconductivity, University of Houston, Houston, Texas 77024, USA

maximize H_V *via* grain boundary strengthening.[20] Solid solutions can likewise stabilize phases at ambient conditions that are otherwise inaccessible. HfB_{12} generally requires high temperature (1600 °C) and pressure (6.5 GPa), but it can be prepared using easier reaction conditions when mixed with other transition metals.[21,22] These examples represent some of the many ways to enhance a compound's mechanical properties using an empirical understanding of solid state chemistry.

Computation-based methods including machine learning, molecular dynamics, and density functional perturbation theory have also been used to study hard materials.[14] For example, machine learning models are capable of directly and quantitatively predicting H_V at room temperature and high temperature using experimentally measured hardness values reported in the literature as the training data set.[23,24] Research has shown that machine learning can further balance a material's hardness and ductility by also modeling fracture toughness.[25,26] Million atom molecular dynamics (MD) simulations provided a route to model deformation mechanism upon indentation and generated calculated H_V values that adequately agree with experimental results.[14] MD simulations are also helpful for probing a material's tendency to retain hardness at elevated temperatures. Researchers have additionally employed more computationally expensive approaches to discover complex hard materials by employing density functional theory (DFT).[14] For instance, the bulk (B) and shear (G) moduli can be calculated with DFT and then entered into semi-empirical models to predict hardness.[27–29] DFT-based techniques can likewise be combined with powerful structure prediction methods like Crystal Structure Analysis by Particle Swarm Optimization (CALYPSO)[30] to predict thermodynamically stable and metastable hard materials.[31] Finally, crystal orbital Hamilton population (COHP) calculations can be used to optimize bonding by varying the valence electron count (VEC) en route to materials with stronger chemical interactions.[32,33] The observed change in the occupied bonding states can then be correlated with the bond strength and ultimately the experimentally measured H_V.

The work presented herein considers the idea of combining both the classical, empirical, experimental-based methods for hard materials discovery and optimization with the computational-based approaches. First, solid solutions with differing electron densities are tested to vary the hardness, and then the electronic structure is analyzed to tune the chemical bonding. This information is ultimately used in tandem to optimize H_V. The system employed to demonstrate this approach is $Sc_2(Ru_{5-x}TM_x)B_4$ (TM = Ta, W, Re, Os, and Ir). This phase is suitable for this study because multiple elements and electron densities can be achieved through TM solid solution formation.[34,35] The initial substitution of Ru for isovalent Os in $Sc_2(Ru_{5-x}Os_x)B_4$ (x = 1.0–5.0) systematically changes the electron density while varying the VEC by exchanging the 5d transition metal modulates the Fermi level as a way to access an electronically advantageous pseudogap and optimize the bonding. The changes in crystal chemistry and electronic structure are subsequently connected to the materials' Vickers hardness. Finally, DFT calculated stress–strain curves provide fundamental insight into the composition-property

relationship necessary to improve the design criteria for developing novel hard materials.

Experimental and computational methods

Synthesis and characterization

Samples of $Sc_2Ru_5B_4$, $Sc_2(Ru_{5-x}Os_x)B_4$ (x = 1–5), and $Sc_2(Ru_4TM)B_4$ (TM = Ta, W, Re, and Ir) were prepared by arc melting the elements in the desired stoichiometric ratios under flowing argon on a water-cooled copper hearth. The starting materials, Sc (HEFA Rare Earth Canada Co. Ltd, 99.999%), W (Alfa Aesar, 99.9%), Os (Alfa Aesar, 99.95%), Ru (Alfa Aesar, 99.95%), Ta (Alfa Aesar, 99.98%), Re (Alfa Aesar, 99.997%), Ir (Alfa Aesar, 99.95%), and crystalline boron (Alfa Aesar, 98%) were weighed out (total mass $\approx$ 0.20 g), pressed into 6 mm pellets, and melted using a current of 25 A to 90 A (depending on the TM) until homogenous melting occurred. The ingots were flipped and remelted at least twice to ensure sample homogeneity. The weight loss after arc melting each sample was <5%. Additional synthesis with excess boron loaded did not improve phase purity or reduce the presence of the secondary phases.

The ingots were split into two pieces. One half was crushed, and single crystals from two of the samples ($Sc_2Ru_5B_4$ and $Sc_2(Ru_4Re)B_4$) were picked with the aid of a ZEISS Stemi 508 optical microscope. Single-crystal data were collected on a Bruker Apex II platform diffractometer fitted with a 4K CCD APEX II detector and a Mo Kα radiation source. Data for $Sc_2Ru_5B_4$ were acquired at 296 K using six sets (2266 frames total) of Omega scans at different Phi settings, with scan widths of 0.5° in ω and an exposure time of 30 s frame^{-1}. Reflections for $Sc_2(Ru_4Re)B_4$ were obtained at 296 K using a narrow-frame algorithm with scan widths of 0.3° in ω and an exposure time of 30 s frame^{-1} (3 sets of 424 frames). The data were integrated with the Bruker Apex II program, and the intensities were corrected for polarization, Lorentz factor, air absorption, and absorption from the difference in path length through the faceplate of the detector. TWINLABS[36] was used to scale the data and apply an absorption correction. The ShelXle program package (version 6.12)[37] was used for structure solution and refinement of both compounds, with a full-matrix least-squares on Fo^2. The crystal of $Sc_2(Ru_4Re)B_4$ was twinned and integrated as such using Bruker Nonius SAINT. The single-crystal refinement statistics, refined atomic positions, and refined harmonic displacement parameters are provided in Tables S1–S3 (ESI†), respectively. The final crystal structure solutions, in CIF format, have been sent to The Cambridge Crystallographic Data Centre (CCDS) and can be obtained from the CCDC using the depository numbers 2118063 ($Sc_2Ru_5B_4$) and 2118062 ($Sc_2(Ru_4Re)B_4$).

The remainder of this first half was ground into a fine powder with a CerCo Diamonite™ mortar and pestle for powder X-ray diffraction analysis using a PANalytical X'Pert powder diffractometer equipped with Cu Kα radiation (λ = 1.54184 Å). The diffractograms were analyzed by the Le Bail refinement

This journal is © The Royal Society of Chemistry 2022

J. Mater. Chem. C, 2022, **10**, 1488–1497 | **1489**

method performed with the General Structure Analysis System (GSAS) software and the EXPGUI interface.[38,39] VESTA was used to visualize the crystal structures.[40]

The other half of the ingots were used for Vickers micro-indentation measurements. The samples were mounted in EpoxiCure™ 2 Epoxy Resin and then polished using a Diamond polishing plate, SiC polishing plates (800–1200 grit), 7 μm, 3 μm, and 1 μm diamond paste until a mirror finish was obtained. An average of ten indentations at 0.49 N (50 kgf) load and five indentations for 0.98, 1.96, 2.94, and 4.9 N (100, 200, 300, and 500 kgf) loads were made using a LECO AMH55, LM810AT Vickers microhardness indenter. The indentations were analyzed using the LECO Cornerstone AMH55 L software to calculate H_V.

The surface morphology of the mounted, polished ingots was also analyzed using a JEOL 6330F field emission scanning electron microscope (FE-SEM) with an emission current of 12 μA and an accelerating voltage of 15 eV. The micrographs were used to analyze the elemental distribution, while the approximate composition was analyzed using energy-dispersive X-ray spectroscopy (EDS). The epoxy surfaces were coated with colloidal graphite paste before analysis to minimize charging.

Density functional theory

The electronic structure of $Sc_2Ru_5B_4$ and $Sc_2(Ru_4TM)B_4$ (TM = Ta, W, Mo, Re, Os, and Ir) was obtained using DFT. These calculations employed the Vienna *ab initio* simulation package (VASP),[41,42] which is a plane-wave basis set with projector-augmented-wave (PAW) pseudopotentials used to describe the electronic wave functions.[43] The Perdew–Burke–Ernzerhof generalized gradient approximation (PBE-GGA) functional was applied to account for exchange and correlation.[44] The energy cutoff was set to 500 eV, with the electronic and ionic convergence criterion set to 1×10^{-8} eV and 1×10^{-6} eV, respectively. A Monkhorst–Pack k-point grid with a minimum of 1000 k-points/atom was used to ensure correct sampling of the first Brillouin zone.[45] The dynamic stability of the converged structures was checked with phonon dispersion calculations generated using the PHONOPY package.[46] These calculations employed the modified Parlinski–Li–Kawazoe *ab initio* force constant method.[46] The force constant matrix was constructed using the Hellmann–Feynman forces obtained by VASP calculations on a $1 \times 1 \times 2$ supercell with symmetry independent atoms displaced by ±0.02 Å.

The calculations of the substitutional analogs required a multi-step process to evaluate the site preference for transition metal atoms in $Sc_2(Ru_4TM)B_4$ (TM = Ta, W, Re, Os, and Ir). First, all symmetry operations were removed from the $Sc_2Ru_5B_4$ parent crystal structure. Each Ru atom was then systematically replaced with the corresponding transition metal atom producing ten unique structures with a composition of $Sc_2(Ru_{4.5}TM_{0.5})B_4$. Every structure was then optimized, and the models with the lowest total energy were identified. Once the substitutional site preference for each TM was identified, compounds with the composition $Sc_2(Ru_4TM)B_4$ were generated by calculating $1 \times 1 \times 2$ supercells using the "Supercell" software.[47] Twelve models for each solid solution were optimized, and the lowest energy models were determined. The energetic difference between the

generated supercell models for each solid solution was <25 meV per atom. Nevertheless, the calculations indicate the lowest total energy model places the TM atom on Wyckoff site 4g, which is in agreement with the single-crystal structure solution for $Sc_2(Ru_4Re)B_4$ (Table S1, ESI†). The exception is when TM = Ir, which showed a calculated site preference where Ir will occupy the 2c Wyckoff site. The lowest total energy models for $Sc_2(Ru_4TM)B_4$ were selected for subsequent DOS and COHP analysis.

Finally, stress–strain calculations were performed to determine the ideal strength of $Sc_2Ru_5B_4$ and $Sc_2(Ru_4TM)B_4$. The unit cells were strained incrementally with a 0.02 Å step size for all stress–strain calculations.[48,49] The uniaxial tensile stress–strain curves were calculated along six high symmetry crystallographic directions, while uniaxial shear stress–strain curves were calculated by applying shear deformation on 26 different slip systems. The resulting stress and strain values were plotted to generate tensile and shear stress–strain curves for $Sc_2(Ru_4TM)B_4$.

Results and discussion

Synthesis and characterization of $Sc_2Ru_5B_4$

The preparation of $Sc_2Ru_5B_4$ was achieved by arc melting the elements in the desired ratios. The crystal structure of $Sc_2Ru_5B_4$, shown in Fig. 1a, was first published by Rogol in 1984 and reported to adopt space group $P2/m$ (space group no. 10) with a monoclinic angle of only $\beta = 90.01(7)°$.[34] An initial analysis of the powder X-ray diffractograms for the sample here did not indicate monoclinic peak splitting. Therefore, single-crystal X-ray diffraction was first used to re-examine the crystal
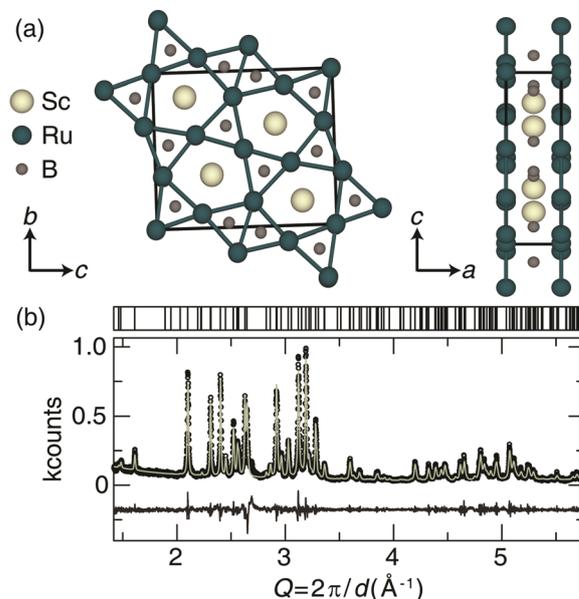
Fig. 1 (a) Single-crystal structure of orthorhombic $Sc_2Ru_5B_4$, where scandium is cream, ruthenium is teal, and boron is dark gray shown along the a-direction (left) and along the b-direction (right). (b) Le Bail refinement of $Sc_2Ru_5B_4$. Black circles represent the measured data, the refinement fit is in cream and the black line represents the difference.

1490 | *J. Mater. Chem. C*, 2022, **10**, 1488–1497

This journal is © The Royal Society of Chemistry 2022

structure of the newly prepared sample. The resulting single-crystal crystallographic data are provided in Table S1 (ESI†). Indeed, the new crystal structure solution shows that $Sc_2Ru_5B_4$ adopts a primitive orthorhombic crystal structure (space group *Pbam*; no. 55) that is nearly identical to the previously published structure, although all angles are now 90° and the bond lengths are slightly different. The unit cell still consists of layers of ruthenium atoms forming a planar pentagonal- and trigonal-connected network. Between these layers sit the Sc and B atoms. The nonregular pentagonal Ru prisms are edge-connected, and scandium resides in the center of the pentagonal Ru-prisms, while the boron occupies the center of trigonal prisms formed by the Ru layers. The refined powder X-ray diffractogram of $Sc_2Ru_5B_4$, displayed in Fig. 1b, indicates the product is nearly phase pure with only minor unidentified impurities. The unit cell parameters of the experimentally refined powder data for $Sc_2Ru_5B_4$ are a = 8.4865(2) Å, b = 2.9930(1) Å, c = 9.9714(2) Å, in agreement with the single-crystal refinement.

The bulk elemental distribution of $Sc_2Ru_5B_4$ in the product was also evaluated by analyzing the backscattered electron (BSE) micrographs. Sample homogeneity is essential for obtaining reliable Vickers microhardness data and should be confirmed before indentation. The polished sample contained the target phase and a minor secondary phase as a lighter region in the BSE. Checking the chemical composition of the backscattered images (Fig. S1a, ESI†) by EDS analysis shows the darker region of the sample is the target phase, $Sc_2Ru_5B_4$, with an estimated transition metal ratio of $Sc_{1.92(2)}Ru_{5.08(2)}$. Lighter elements like boron are notoriously tricky to analyze by EDS quantitatively; therefore, only the transition metal ratios have been estimated here.[50] The lighter regions of the sample appear to correspond to a binary Ru–B phase.

Acquiring the applied load hardness curve is necessary to capture the relationship between composition and hardness, which provides insight into the indentation size effect of this phase.[51] Therefore, Vickers microindentation measurements were performed at five applied loads. The hardness values for $Sc_2Ru_5B_4$, plotted in Fig. 2, indicate the material is reasonably hard with an H_V of 23(2) GPa at 0.49 N applied load. The hardness then decreases $\approx 40\%$ from 0.49 N load to 4.9 N load. This response is comparable with most Vickers hardness measurements in accordance with the indentation size effect.[23,52] The hardness of $Sc_2Ru_5B_4$, although not superhard, is comparable to industry-standard materials like ZrC[53] and TaB_2,[54] which have H_V values of ≈ 22 GPa and ≈ 26 GPa, respectively, at 0.49 N. Given the reasonably impressive mechanical properties of this phase with the comparatively lighter elements, applying chemical substitution through solid solution formation could be viable for enhancing the hardness of this material following the conventional understanding of hardness in borides.[2]

Improving the hardness in $Sc_2(Ru_{5-x}Os_x)B_4$ *via* solid solution

Transition metals with higher electron density can be incorporated into $Sc_2Ru_5B_4$ to produce solid solutions with enhanced
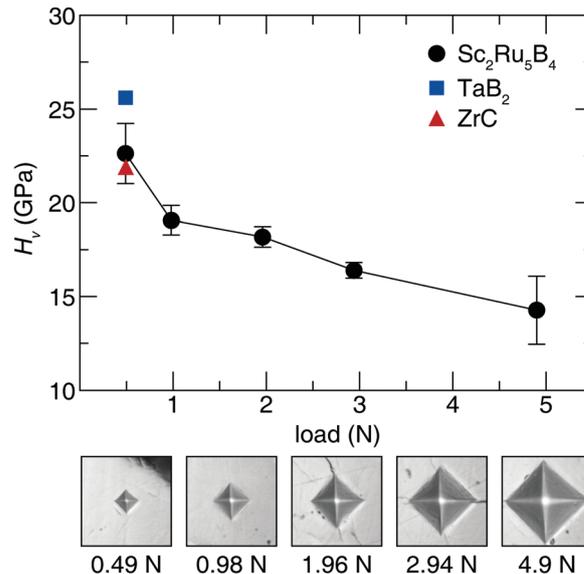

Fig. 2 Vickers microindentation (H_V) measurements of $Sc_2Ru_5B_4$ from low (0.49 N) to high (4.9 N) load and TaB_2 and ZrC at low (0.49 N) load. Error bars correspond to the average error of multiple independent measurements. Representative indentations from each applied load are shown below the plot.

hardness following traditional design rules. Substituting Ru atoms with isovalent Os atoms following $Sc_2(Ru_{5-x}Os_x)B_4$ (x = 1–5) was achieved by arc melting the appropriate ratios of elements to increase the electron density. The refined powder X-ray diffractograms, plotted in Fig. 3a, demonstrate that when x = 1, 2, and 3, the product was obtained nearly phase pure with minor unidentified impurities. Further increasing the Os content in $Sc_2(Ru_{5-x}Os_x)B_4$ (x = 4 and 5) resulted in the formation of the target phase and small peaks indexing to Os and other minor unidentified impurities. Refinements of all five products show they are isostructural with $Sc_2Ru_5B_4$, while substituting Ru atoms for larger Os atoms increases the lattice parameters shifting the diffraction peaks to lower Q-spacing. This trend is confirmed by plotting the refined unit cell volume, which shows a linear increase in volume following Vegard's law (Fig. 3b).

Sample homogeneity and elemental composition of $Sc_2(Ru_{5-x}Os_x)B_4$ were again determined by analyzing the BSE micrographs. The metallic ratios were obtained *via* EDS have nominal compositions of $Sc_{2.53(3)}Ru_{3.70(1)}Os_{0.77(4)}$, $Sc_{2.5(1)}Ru_{2.8(1)}Os_{1.7(4)}$, $Sc_{2.48(4)}Ru_{1.90(3)}Os_{2.62(3)}$, $Sc_{2.3(2)}Ru_{0.9(1)}Os_{3.8(1)}$, and $Sc_{2.4(2)}Os_{4.6(2)}$. Although there are small inconsistencies between the experimental and nominal loaded transition metal ratios, the semi-quantitative analysis supports the incorporation of Os as desired. EDS analysis of the $Sc_2(RuOs_4)B_4$ and $Sc_2Os_5B_4$ samples reveal the presence of Ru-rich secondary phases—$Sc_{0.8(1)}Ru_{3.8(2)}Os_{1.0(1)}$ and $Sc_{1.0(1)}Ru_{1.4(2)}Os_{1.3(1)}$ in $Sc_2(Ru_4Os)B_4$ and $Sc_2(Ru_3Os_2)B_4$, and an Os-rich secondary phase of $Sc_{3.1(1)}Ru_{1.0(2)}Os_{4.4(2)}$ in $Sc_2(Ru_2Os_3)B_4$. There are also Os inclusions in both samples. Nevertheless, large regions of the target phases in all samples are present, allowing indentation measurements. Fig. 3c shows the resulting Vickers microindentation measurements for the solid solutions $Sc_2(Ru_{5-x}Os_x)B_4$ at 0.49
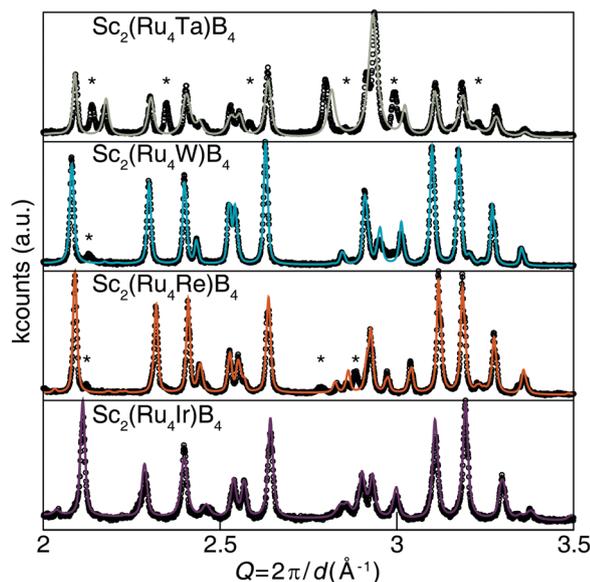
This journal is © The Royal Society of Chemistry 2022

J. Mater. Chem. C, 2022, **10**, 1488–1497 | **1491**

Fig. 3 (a) Powder X-ray diffractograms of the solid solution $Sc_2(Ru_{5-x}Os_x)B_4$ (x = 1–5). (b) The refined volume determined from Le Bail refinements as a function of x follows Vegard's law. (c) Vickers microindentation (H_V) measurements of $Sc_2(Ru_{5-x}Os_x)B_4$ at low load (0.49 N) and high load (4.9 N).

and 4.9 N loads. The hardness increases as Os content increases for both applied loads. At high load the Vickers microhardness increases moderately from 14.3(2) GPa at x = 0 to 17.1(1) GPa at x = 5. The low load hardness increases nearly 25% with hardness values of 23(2) GPa at x = 0 and 29(1) GPa at x = 5.

These data support that the hardness of $Sc_2Ru_5B_4$ can be raised by substituting Ru for Os atoms. Substituting isovalent Os for Ru atoms does not affect the overall electronic structure of the compounds. Thus, the observed increase in hardness of the continuous solid solution $Sc_2(Ru_{5-x}Os_x)B_4$ stems solely from the difference in electron density between the Os and Ru atoms. This design principle is utilized to increase the hardness of various boride systems and is demonstrated here.

Influence of 5d transition metal substitution on vickers hardness of $Sc_2(Ru_{5-x}TM_x)B_4$

Incorporating elements with high electron density through solid solutions is an accepted design strategy route to increase transition metal borides' hardness. An alternative electronic-based approach can also be used to increase the hardness.[14] Accordingly, the rigid band approximation was used to identify other 5d transition metals that may be substituted into the structure to increase hardness. Analyzing the electronic structure of $Sc_2(Ru_4Os)B_4$ shows the DOS calculated with DFT, plotted in Fig. 4a, has a significant number of bands crossing the Fermi level supporting metallic behavior. Interestingly, a pseudogap is present just below the Fermi level (E_F) and could be accessed to increase phase stability.[55] A shift of the E_F towards the pseudo-gap centered at -0.36 eV can be achieved by reducing the valence electron count from 116 VEC to 114 VEC.

The changes in chemical bonding character as a function of VEC can also be correlated to mechanical properties.[32,33] Analyzing the calculated crystal orbital Hamilton population

Fig. 4 (a) DOS curve of $Sc_2(Ru_4Os)B_4$. The Fermi level is plotted for $Sc_2(Ru_4Os)B_4$. The corresponding VEC is provided for each transition metal substituted compound according to the rigid band approximation. The B and Os states below the Fermi level are filled in dark gray and yellow, respectively. (b) $-$COHP curve of $Sc_2(Ru_4Os)B_4$ plotting the sum (total) of all pairwise interactions and Ru–Ru contacts with an interatomic separation between 1 Å to 4 Å. The states occupied by electrons are shown filled in light gray, whereas the occupied Ru–Ru interactions are filled in blue.

($-$COHP) curves, which decomposes the band-structure energy into pairwise bonding and antibonding contributions, for $Sc_2(Ru_4Os)B_4$ indicates E_F falls in a region dominated by anti-bonding interactions stemming primarily from the Ru–Ru interactions. Applying the same rigid band approximation shows that reducing the VEC should decrease the occupation

1492 | *J. Mater. Chem. C*, 2022, **10**, 1488–1497

This journal is © The Royal Society of Chemistry 2022

Fig. 5 Powder X-ray diffractograms of the solid solution $Sc_2(Ru_4TM)B_4$ (TM = Ta, W, Re, and Ir) and the associated Le Bail refinements.

Fig. 6 Vickers microindentation measurements of (a) $Sc_2(Ru_4Ta)B_4$ (b) $Sc_2(Ru_4W)B_4$. (c) $Sc_2(Ru_4Re)B_4$ (d) $Sc_2(Ru_4Ir)B_4$ from low (0.49 N) load to high load (4.9 N).

of antibonding orbitals, leading to an optimized electron count when VEC ≈ 114.

The desired valence electron counts were experimentally obtained by synthesizing $Sc_2(Ru_4TM)B_4$ (TM = Ta, W, Re, and Ir) with the specific transition metals used to vary the VEC. Fig. 5 illustrates that all compounds, except $Sc_2(Ru_4Ta)B_4$, are nearly phase pure based on powder X-ray diffraction with only minor unidentified peaks. Refining the X-ray diffractograms using the Le Bail method confirms that the solid solutions are all isostructural to the $Sc_2Ru_5B_4$ parent phase. The refined lattice parameters are provided in Table S4 (ESI†). The TM solubility limit was found to be near 20% for these 5d transition metals; every attempt to increase the transition metal concentration beyond $x = 1$ resulted in discernable impurity peaks in their corresponding diffractograms. Examining the BSE (Fig. S1b–f, ESI†) and resulting EDS data revealed the nominal transition metal ratios for each solid solution as $Sc_{2.38(4)}Ru_{4.3(1)}Ta_{0.37(4)}$, $Sc_{2.44(3)}Ru_{3.8(1)}W_{0.8(1)}$, $Sc_{2.52(3)}Ru_{3.79(2)}Re_{0.69(4)}$, and $Sc_{2.50(2)}Ru_{3.9(1)}Ir_{0.6(1)}$. Despite the minor discrepancies between the experimental and nominal loaded transition metal ratios, the refined diffractograms in combination with EDS results verify that 5d transition metals can be substituted into $Sc_2Ru_5B_4$ without the emergence of significant secondary phases, except for when TM = Ta. The electronic structure supports the synthetic challenges associated with preparing $Sc_2(Ru_4Ta)B_4$ as a pure phase material. The Fermi level of $Sc_2(Ru_4Ta)B_4$ falls below the pseudogap on a large shoulder in the DOS, suggesting electronic instabilities for this composition. Thus, the VEC of 110 corresponds to the lower substitution limit in $Sc_2(Ru_4TM)B_4$.

The Vickers hardness data, plotted in Fig. 6, was determined for $Sc_2(Ru_4TM)B_4$ (TM = Ta, W, Re, and Ir). The $Sc_2(Ru_4TM)B_4$ hardness first increases at low applied load, going from Os to Re. This follows the reduction of the VEC to 114 and placing E_F in the minimum of the pseudogap. It also corresponds with a
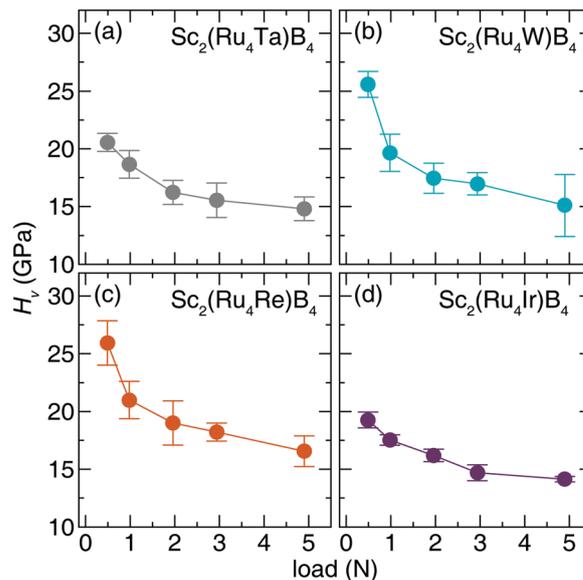
reduction in the number of occupied antibonding interactions within the crystal structure. Further reducing the VEC by substituting W into the structure shows virtually no change in the H_V stemming from a similar electronic structure between TM = Re and TM = W. The percent loss in hardness going from $Sc_2(Ru_4Re)B_4$ to $Sc_2(Ru_4Ta)B_4$, however, is $\approx 21\%$. On the other side, a similar drop in hardness of $\approx 26\%$ is also observed from $Sc_2(Ru_4Re)B_4$ to $Sc_2(Ru_4Ir)B_4$. The significant drop in hardness in these compounds can be related to the expected Fermi level position moving from a deep pseudogap for $Sc_2(Ru_4Re)B_4$ to shoulders in the DOS for $Sc_2(Ru_4Ta)B_4$ and $Sc_2(Ru_4Ir)B_4$. Moreover, when TM = Ir, even more electrons are in the system populating antibonding orbitals. These data confirm that the hardness of $Sc_2Ru_5B_4$ can be increased by tuning its electronics through 5d transition metal substitution.

Furthermore, the Vicker's microhardness of $Sc_2(Ru_{5-x}TM_x)B_4$ (TM = Ru, Re, and Os) can be compared to the hardness of previously reported borides, shown in Table 1. This analysis focuses particularly on systems with a similar boron content, providing context for the experimental data reported here and illustrating the diversity of mechanical responses in borides. For instance, the hardness of WB_4 at 0.49 N and the solid solutions $Zr_{0.5}W_{0.5}B_4$ and $W_{0.93}Ta_{0.02}Cr_{0.05}B_4$ far exceed the measured hardness values of $Sc_2(Ru_{5-x}TM_x)B_4$. $Sc_2Os_5B_4$ still has a higher hardness than many other reported ternary tetraborides. In fact, the hardness of $Sc_2(Ru_{5-x}TM_x)B_4$ at 0.49 N load lies between the softest ($ErRh_4B_4$) and hardest ($YCrB_4$) ternary tetraborides, which have a hardness of ≈ 11 GPa and ≈ 38 GPa at 0.98 N and 0.49 N loads, respectively. These results demonstrate that $Sc_2(Ru_{5-x}TM_x)B_4$ has reasonably high hardness values compared to other ternary tetraborides and reaffirms the capability to discover hard borides in the ternary phase space.

This journal is © The Royal Society of Chemistry 2022

J. Mater. Chem. C, 2022, **10**, 1488–1497 | **1493**

Table 1   Vicker's microhardness of select tetraborides

Compound	$H_{V,0.49N}$ (GPa)	$H_{V,4.9N}$ (GPa)	Ref.
Cr_3B_4	24	—	56
WB_4	43	28	8
$Zr_{0.5}W_{0.5}B_4$	46	33	57
$W_{0.93}Ta_{0.02}Cr_{0.05}B_4$	57	32	58
Cr_3AlB_4	19	15	59
$ErRh_4B_4$	11^a	—	60
$YCrB_4$	38	24	61
$Sc_2Ru_5B_4$	23	14	This work
$Sc_2Os_5B_4$	29	17	This work
$Sc_2(Ru_4Re)B_4$	26	17	This work

^{a} H_V was obtained at 0.98 N load.

Correlating hardness and shear stress of $Sc_2(Ru_4TM)B_4$

The structural-mechanical properties of $Sc_2Ru_5B_4$ and $Sc_2(Ru_4TM)B_4$ (TM = Ta, W, Re, Os, and Ir) were further investigated using *ab initio* stress–strain calculations to understand the evolution of the materials' response. Stress–strain evaluating various crystallographic directions and planes under tensile and shear strain curves illustrate the relationship between stress and strain by gradually increasing the deforming force (stress) on the sample until failure (strain).[62]

The uniaxial tensile stress–strain curve for the highest and lowest stress symmetry directions of $Sc_2Ru_5B_4$ are visualized in Fig. 7a. The observed stress varies as the crystal structure is strained along different crystallographic orientations. The anisotropic response to tension coincides with the anisotropy observed in the orthorhombic crystal structure of $Sc_2Ru_5B_4$. Upon the initial deformation, the tensile stress–strain curves experience a brief, near-linear increase until 0.1 strain. As the applied strain is increased, the stress in both directions begins to vary. For example, the lowest stress that $Sc_2Ru_5B_4$ can
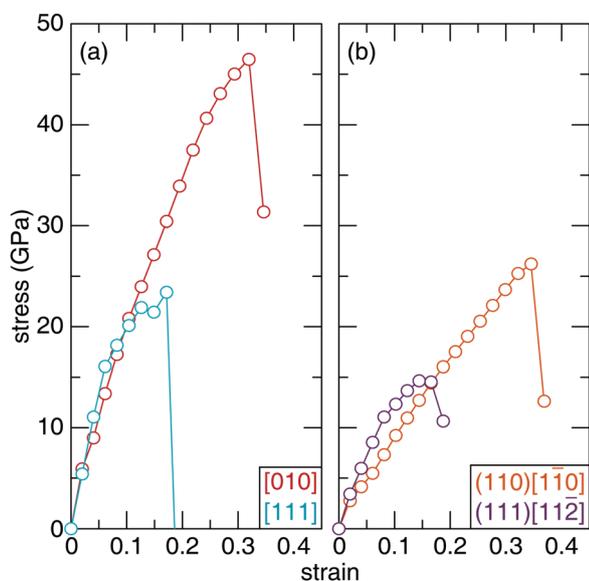
withstand occurs along the [111] direction, which reaches a maximum of ≈ 23 GPa at 0.17 strain. The highest tensile strength occurs for the [010] direction reaching ≈ 46.5 GPa at 0.32 strain. These data resemble the general expected trend for tensile stress–strain curves of polycrystalline materials.[63] The complete tensile strength calculations for $Sc_2Ru_5B_4$ are provided in Table S5 (ESI†).

The mechanical behavior of $Sc_2Ru_5B_4$ was also evaluated under uniaxial shear stress for 26 different crystallographic slip planes. Since Vickers hardness indentations are governed by plastic rather than elastic deformation, the irreversible motion of atoms occurs *via* shear stress.[64] The weakest slip systems correspond to the failure of a material and thus, can be correlated to the experimental Vickers microhardness.[65] The complete shear strength calculations for $Sc_2Ru_5B_4$ are provided in Table S6 (ESI†). The weakest shear stress in $Sc_2Ru_5B_4$, shown in Fig. 7b, occurs for the $(111)[11\bar{2}]$ slip plane with the stress of ≈ 15 GPa at 0.14 strain. Conversely, the strongest shear strength is achieved for the $(110)[1\bar{1}0]$ slip plane with a value of ≈ 26 GPa at 0.35 strain. To put these values into perspective, the softest shear stress of OsB_2 is 9.2 GPa at 0.2 strain in the $(001)[100]$ direction.[66] Both OsB_2 and $Sc_2Ru_5B_4$ have relatively similar shear stress and thus, should have similar mechanical properties. Indeed, both compounds are considered hard materials with Vickers hardness within the standard deviation of one another.[67]

A similar analysis can be applied to the calculated uniaxial shear stress–strain curves for $Sc_2(Ru_4TM)B_4$. The maximum shear stress of the softest shear slip system for each solid solution and their corresponding hardness values are plotted in Fig. 8. The complete results for shear stress of the solid solution $Sc_2(Ru_4TM)B_4$ are compiled in Tables S7–S11 (ESI†). These shear stress–strain calculations indicate that the solid solution $Sc_2(Ru_4Re)B_4$ achieves the highest stress of the weakest slip system along the $(100)[011]$, which has ideal stress of ≈ 19 GPa at 0.16 strain. Moreover, the observed shear stress of $Sc_2(Ru_4W)B_4$ for the $(010)[\bar{1}00]$ is nearly identical to $Sc_2(Ru_4Re)B_4$ with a $<1\%$ difference. Any additional variation to the transition metal in $Sc_2(Ru_4TM)B_4$ (*i.e.*, TM = Ta, Os, Ir) will result in a significant drop in stress. For instance, the softest shear plane in $Sc_2(Ru_4Ir)B_4$ is achieved for the $(010)[101]$ shear slip system with ideal stress of ≈ 8.9 GPa. Comparing the max stress of the weakest slip system in $Sc_2Ru_5B_4$ with the shear stress values of $Sc_2(Ru_4TM)B_4$ indicates the ideal stress of $Sc_2Ru_5B_4$ is slightly higher than $Sc_2(Ru_4Os)B_4$ with a $\approx 3\%$ difference.

An assessment of the weakest slip systems for each solid solution shows that when TM = Ta, W, Re, or Ir, the softest planes occur along the faces of the unit cells. The weakest planes occur along the body diagonal for the isovalent compounds, $Sc_2(Ru_4Os)B_4$ and $Sc_2Ru_5B_4$. However, considering the next softest plane for the latter two compositions, the softest planes also reside along a face. The similarity between the softest shear stress planes is expected since these compositions differ by only a low concentration of transition metal atoms. Furthermore, a clear trend is observed for the calculated shear stress of the solid
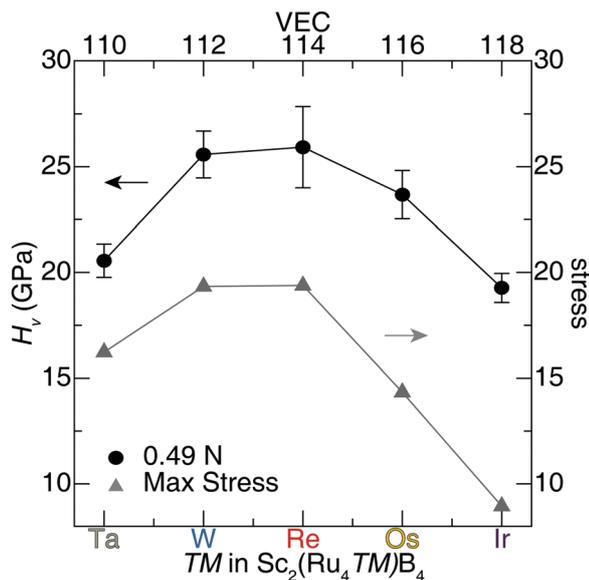

Fig. 7   Calculated stress–strain curves for $Sc_2Ru_5B_4$ (a) Stress–strain curves for various crystallographic directions under applied tension. (b) Stress–strain curves for the hardest and softest shear systems.

1494 | *J. Mater. Chem. C*, 2022, **10**, 1488–1497

This journal is © The Royal Society of Chemistry 2022

Fig. 8 Vickers hardness and shear stress of softest slip systems in $Sc_2(Ru_4TM)B_4$.

reaffirms the capability to approximate general trends of the experimental hardness of $Sc_2(Ru_4TM)B_4$. The approach developed in this work confirms that manipulating the position of the Fermi level is a practical technique to enhance the hardness of materials, especially when combined with classical consideration of materials development and reinforces the importance of validating computational modeling with experimental results.

Conflicts of interest

There are no conflicts to declare.

Acknowledgements

References

1 R. W. Cumberland, M. B. Weinberger, J. J. Gilman, S. M. Clark, S. H. Tolbert and R. B. Kaner, Osmium Diboride, An Ultra-Incompressible, Hard Material, *J. Am. Chem. Soc.*, 2005, **127**, 7264–7265.

2 M. T. Yeung, R. Mohammadi and R. B. Kaner, Ultraincompressible, Superhard Materials, *Annu. Rev. Mater. Res.*, 2016, **46**, 465–485.

3 N. Kalfagiannis, G. Volonakis, L. Tsetseris and S. Logothetidis, Excess of Boron in TiB₂ Superhard Thin Films: A Combined Experimental and Ab Initio Study, *J. Phys. D: Appl. Phys.*, 2011, **44**, 1–7.

4 F. W. Vahldiek, Electrical Resistivity, Elastic Modulus, and Debye Temperature of Titanium Diboride, *J. Less-Common Met.*, 1967, **12**, 202–209.

5 L. Bsenko and T. Lundstrom, The High-Temperature Hardness of ZrB₂ and HfB₂, *J. Less-Common Met.*, 1974, **34**, 273–278.

6 H. Chung, M. B. Weinberger, J. B. Levine, A. Kavner, J. Yang, S. H. Tolbert and R. B. Kaner, Synthesis of Ultra-Incompressible Superhard Rhenium Diboride at Ambient Pressure, *Science*, 2007, **316**, 436–439.

7 N. Dubrovinskaia, L. Dubrovinsky and V. L. Solozhenko, Comment on Synthesis of Ultra-Incompressible Superhard Rhenium Diboride at Ambient Pressure, *Science*, 2007, **318**, 1550d.

8 R. Mohammadi, A. T. Lech, M. Xie, B. E. Weaver, M. T. Yeung, S. H. Tolbert and R. B. Kaner, Tungsten Tetraboride, An Inexpensive Superhard Material, *Proc. Natl. Acad. Sci. U. S. A.*, 2011, **108**, 10958–10962.

9 J. B. Levine, S. H. Tolbert and R. B. Kaner, Advancements in the Search for Superhard Ultra-Incompressible Metal Borides, *Adv. Funct. Mater.*, 2009, **19**, 3519–3533.

solution $Sc_2(Ru_4TM)B_4$, such that the maximum stress increases with transition metal substitution from Ta to Re in $Sc_2(Ru_4TM)B_4$ and then experiences a significant drop from Re to Ir substitution. This trend is also evident in the experimental hardness values of $Sc_2(Ru_4TM)B_4$, where the hardness decreases as you shift away from the ideal composition, $Sc_2(Ru_4Re)B_4$. Although shear stress values are slightly lower than anticipated, an apparent correlation emerges between the maximum stress of $Sc_2(Ru_4TM)B_4$ and their corresponding Vickers hardness. These results reinforce the capability to predict relative experimental hardness values of solid solutions by calculating shear stress–strain curves *via* DFT.

Conclusions

In summary, combining computational modeling with experimental methods remains a viable option for strengthening the hardness of a material. $Sc_2Ru_5B_4$ is ideal to evaluate such an approach because of the versatile crystal chemistry inherent in this phase. Vickers microhardness measurements establish that $Sc_2Ru_5B_4$ is a hard material and that its hardness can be increased by substituting Ru atoms for Os. This somewhat expected result follows conventional design rules for hard materials where the increasing electron density of a system should improve the mechanical properties. This work also shows that exchanging Os for a different 5d transition metal can also increase the material's hardness. The rationale behind these results is elucidated by analyzing a DFT-generated DOS curve of $Sc_2(Ru_4Os)B_4$. The Fermi level of $Sc_2(Ru_4Os)B_4$ lies on a disadvantageous peak, and a bonding analysis reveals the occupation of antibonding metal–metal contacts. Modulating the composition to access a more energetically favorable pseudogap by tuning the VEC results in improved hardness. Moreover, analyzing DFT calculated shear stress–strain curves

10 G. Akopov, M. T. Yeung and R. B. Kaner, Rediscovering the Crystal Chemistry of Borides, *Adv. Mater.*, 2017, **29**, 1–29.

11 Y. B. Kuz'ma, N. S. Bilonizhko, S. I. Mykhalenko, G. F. Stepanchikova and N. F. Chaban, The Interaction of Transition and Rare Earth Metals with Boron, *J. Less Common Met*, 1979, **67**, 51–57.

12 G. Akopov, L. E. Pangilinan, R. Mohammadi and R. B. Kaner, Perspective: Superhard Metal Borides: A look Forward, *APL Mater.*, 2018, **6**, 1–6.

13 M. Xie, R. Mohammadi, C. L. Turner, R. B. Kaner, A. Kavner and S. H. Tolbert, Exploring Hardness Enhancement in Superhard Tungsten Tetraboride-Based Solid Solutions Using Radial X-Ray Diffraction, *Appl. Phys. Lett.*, 2015, **107**, 1–5.

14 A. M. Tehrani and J. Brgoch, Hard and Superhard Materials: A Computational Perspective, *J. Solid State Chem.*, 2019, **271**, 47–58.

15 C. T. Liu, C. L. White and J. A. Horton, Effect of Boron on Grain-Boundaries in Ni_3Al, *Acta Metall.*, 1985, **33**, 213–229.

16 A. T. Lech, C. L. Turner, J. Lei, R. Mohammadi, S. H. Tolbert and R. B. Kaner, Superhard Rhenium/Tungsten Diboride Solid Solutions, *J. Am. Chem. Soc.*, 2016, **138**, 14398–14408.

17 J. Gild, Y. Zhang, T. Harrington, S. Jiang, T. Hu, M. C. Quinn, W. M. Mellor, N. Zhou, K. Vecchio and J. Luo, High-Entropy Metal Diborides: A New Class of High-Entropy Materials and a New Type of Ultrahigh Temperature Ceramics, *Sci. Rep.*, 2016, **6**, 1–10.

18 J.-W. Yeh, S. K. Chen, S.-J. Lin, J.-Y. Gan, T.-S. Chin, T.-T. Shun, C.-H. Tsau and S.-Y. Chang, Nanostructured High-Entropy Alloys with Multiple Principal Elements: Novel Alloy Design Concepts and Outcomes, *Adv. Eng. Mater.*, 2004, **6**, 299–303.

19 Y. Zhang, T. T. Zuo, Z. Tang, M. C. Gao, K. A. Dahmen, P. K. Liaw and Z. P. Lu, Microstructures and Properties of High-Entropy Alloys, *Prog. Mater. Sci.*, 2014, **61**, 1–93.

20 S. W. Xin, X. Shen, C. C. Du, J. Zhao, B. R. Sun, H. X. Xue, T. T. Yang, X. C. Cai and T. D. Shen, Bulk Nanocrystalline Boron-Doped VNbMoTaW High Entropy Alloys with Ultrahigh Strength, Hardness, and Resistivity, *J. Alloys Compd.*, 2021, **853**, 1–11.

21 G. Akopov, M. T. Yeung, C. L. Turner, R. L. Li and R. B. Kaner, Stabilization of HfB_{12} in $Y_{1−x}Hf_xB_{12}$ Under Ambient Pressure, *Inorg. Chem.*, 2016, **55**, 5051–5055.

22 J. F. Cannon and P. B. Farnsworth, High Pressure Synthesis of ThB_{12} and HfB_{12}, *J. Less Common Met*, 1983, **92**, 359–368.

23 Z. Zhang, A. Mansouri Tehrani, A. O. Oliynyk, B. Day and J. Brgoch, Finding the Next Superhard Material through Ensemble Learning, *Adv. Mater.*, 2021, **33**, 1–8.

24 Z. Zhang and J. Brgoch, Determining Temperature-Dependent Vickers Hardness with Machine Learning, *J. Phys. Chem. Lett.*, 2021, **12**, 6760–6766.

25 H. Niu, S. Niu and A. R. Oganov, Simple and Accurate Model of Fracture Toughness of Solids, *J. Appl. Phys.*, 2019, **125**, 1–6.

26 E. Mazhnik and A. R. Oganov, A Model of Hardness and Fracture Toughness of Solids, *J. Appl. Phys.*, 2019, **126**, 1–11.

27 N. Miao, B. Sa, J. Zhou and Z. Sun, Theoretical Investigation on the Transition-Metal Borides with Ta_3B_4-Type Structure: A Class of Hard and Refractory Materials, *Comput. Mater. Sci.*, 2011, **50**, 1559–1566.

28 X.-Q. Chen, H. Niu, D. Li and Y. Li, Modeling Hardness of Polycrystalline Materials and Bulk Metallic Glasses, *Intermetallics*, 2011, **19**, 1275–1281.

29 A. L. Ivanovskii, Hardness of Hexagonal AlB_2-Like Diborides of s, p and d Metals from Semi-Empirical Estimations, *Int. J Refract. Hard*, 2013, **36**, 179–182.

30 Y. Wang, J. Lv, L. Zhu and Y. Ma, CALYPSO: A Method for Crystal Structure Prediction, *Comput. Phys. Commun.*, 2012, **183**, 2063–2070.

31 X. Zhang, Y. Wang, J. Lv, C. Zhu, Q. Li, M. Zhang, Q. Li and Y. Ma, First-Principles Structural Design of Superhard Materials, *J. Chem. Phys.*, 2013, **138**, 1–9.

32 J. P. Scheifers, R. D.-T. Nguyen, Y. Zhang and B. P. T. Fokwa, Direct Correlation of Mechanical Hardness and Chemical Bonding in Intermetallic Double Perovskite Borides $Sc_2Ir_{6−x}Pd_xB$, *J. Phys. Chem. C*, 2020, **124**, 26062–26067.

33 J. Zhang, A. M. Tehrani and J. Brgoch, Tailoring the Mechanical Properties of Earth-Abundant Transition Metal Borides via Bonding Optimization, *J. Phys. Chem. C*, 2020, **124**, 4430–4437.

34 P. Rogl, The Crystal Structure of $Sc_2Ru_5B_4$, *J. Solid State Chem.*, 1984, **55**, 262–269.

35 L. P. Salamakha, O. Sologub, B. Stöger, P. F. Rogl, M. Waas, V. B. Kapustianyk and E. Bauer, $ScRu_2B_3$ and Sc_2RuB_6: Borides Featuring a 2D Infinite Boron Clustering, *Inorg. Chem.*, 2017, **56**, 10549–10558.

36 G. M. Sheldrick, *TWINLABS*. University of Göttingen, Göttingen, Germany, 2008.

37 C. B. Hubschle, G. M. Sheldrick and B. Dittrich, ShelXle: A Qt Graphical User Interface for SHELXL, *J. Appl. Cryst.*, 2011, **44**, 1281–1284.

38 B. H. Toby, EXPGUI, A Graphical User Interface for GSAS, *J. Appl. Cryst.*, 2001, **34**, 210–213.

39 B. H. Toby and R. B. Von Dreele, GSAS-II: The Genesis of a Modern Open-Source All Purpose Crystallography Software Package, *J. Appl. Crystallogr.*, 2013, **46**, 544–549.

40 K. Momma and F. Izumi, VESTA 3 For Three-Dimensional Visualization of Crystal, Volumetric and Morphology Data, *J. Appl. Crystallogr.*, 2011, **44**, 1272–1276.

41 G. Kresse and J. Furthmuller, Efficient Iterative Schemes for Ab Initio Total-Energy Calculations Using a Plane-Wave Basis Set, *Phys. Rev. B: Condens. Matter Mater. Phys.*, 1996, **54**, 169–186.

42 G. Kresse and D. Joubert, From Ultrasoft Pseudopotentials to the Projector Augmented-Wave Method, *Phys. Rev. B: Condens. Matter Mater. Phys.*, 1999, **59**, 1758–1775.

43 P. E. Blochl, Projector Augmented-Wave Method, *Phys. Rev. B: Condens. Matter Mater. Phys.*, 1994, **50**, 17953–17979.

44 J. P. Perdew, Density Functional Theory and the Band Gap, *Int. J. Quantum Chem.*, 1985, **28**, 497–523.

45 H. J. Monkhorst and J. D. Pack, Special Points for Brillouin-Zone Integrations, *Phys. Rev. B: Condens. Matter Mater. Phys.*, 1976, **13**, 5188–5192.

1496 | *J. Mater. Chem. C*, 2022, **10**, 1488–1497

This journal is © The Royal Society of Chemistry 2022

46 A. Togo and I. Tanaka, First Principles Phonon Calculations in Materials Science, *Scr. Mater.*, 2015, **108**, 1–5.

47 K. Okhotnikov, T. Charpentier and S. Cadars, Supercell Program: A Combinatorial Structure-Generation Approach for the Local-Level Modeling of Atomic Substitutions and Partial Occupancies in Crystals, *J. Cheminf.*, 2016, **8**, 1–15.

48 Y. Li, J. Hao, H. Liu, S. Lu and J. S. Tse, High-Energy Density and Superhard Nitrogen-Rich B-N Compounds, *Phys. Rev. Lett.*, 2015, **115**, 1–5.

49 M. Zhang, M. Lu, Y. Du, L. Gao, C. Lu and H. Liu, Hardness of FeB_4: Density Functional Theory Investigation, *J. Chem. Phys.*, 2014, **140**, 174505.

50 B. J. Inkson, Scanning Electron Microscopy (SEM) and Transmission Electron Microscopy (TEM) for Materials Characterization. in *Materials Characterization Using Non-destructive Evaluation (NDE) Methods*, ed. E., Ltd, 2016, pp. 17–43.

51 G. M. Pharr, E. G. Herbert and Y. Gao, The Indentation Size Effect: A Critical Examination of Experimental Observations and Mechanistic Interpretations, *Annu. Rev. Mater. Res.*, 2010, **40**, 271–292.

52 J. G. Swadener, E. P. George and G. M. Pharr, The Correlation of the Indentation Size Effect Measured With Indenters of Various Shapes, *J. Mech. Phys. Solids*, 2002, **50**, 681–694.

53 S. E. Landwehr, G. E. Hilmas, W. G. Fahrenholtz, I. G. Talmy and S. G. DiPietro, Microstructure and Mechanical Characterization of ZrC–Mo Cermets Produced by Hot Isostatic Pressing, *Mater. Sci. Eng., A*, 2008, **497**, 79–86.

54 X. Zhang, G. E. Hilmas and W. G. Fahrenholtz, Synthesis, Densification, and Mechanical Properties of TaB_2, *Mater. Lett.*, 2008, **62**, 4251–4253.

55 P. Ravindran and R. Asokamani, Correlation Between Electronic structure, Mechanical Properties and Phase Stability in Intermetallic Compounds, *Bull. Mater. Sci.*, 1997, **20**, 613–622.

56 S. Okada and T. Atoda, Preparation of Single Crystals of a New Boride Cr_2B_3 by the Aluminium-Flux Technique and Some of its Properties, *J. Less Common Met*, 1985, **113**, 331–339.

57 G. Akopov, M. T. Yeung, C. L. Turner, R. Mohammadi and R. B. Kaner, Extrinsic Hardening of Superhard Tungsten Tetraboride Alloys with Group 4 Transition Metals, *J. Am. Chem. Soc.*, 2016, **138**, 5714–5721.

58 R. Mohammadi, M. Xie, A. T. Lech, C. L. Turner, A. Kavner, S. H. Tolbert and R. B. Kaner, Toward Inexpensive Superhard Materials: Tungsten Tetraboride-Based Solid Solutions, *J. Am. Chem. Soc.*, 2012, **134**, 20660–20668.

59 M. Ade and H. Hillebrecht, Ternary Borides Cr_2AlB_2, Cr_3AlB_4, and Cr_4AlB_6: The First Members of the Series $(CrB_2)_nCrAl$ with n = 1, 2, 3 and a Unifying Concept for Ternary Borides as MAB-Phases, *Inorg. Chem.*, 2015, **54**, 6122–6135.

60 T. Shishido, K. Kudou, S. Okada, J. Ye, M. Oku, H. Horiuchi and T. Fukuda, Electrical Resistivity, Oxidation Resistivity and Hardness of Single Crystal Compounds in the Er–Rh–B System, *J. Alloys Compd.*, 1998, **280**, 65–70.

61 G. Akopov, H. Yin, I. Roh, L. E. Pangilinan and R. B. Kaner, Investigation of Hardness of Ternary Borides of the $YCrB_4$, Y_2ReB_6, Y_3ReB_7, and YMo_3B_7 Structural Types, *Chem. Mater.*, 2018, **30**, 6494–6502.

62 D. Roylance, *Stress–Strain Curves, Massachusetts Institute of Technology Study*, Cambridge. 2001.

63 G. N. Haidemenopoulos, *Physical Metallurgy: Principles and Design*, Taylor & Francis Group, Boca Raton. 2018.

64 J. J. Gilman, *Chemistry and Physics of Mechanical Hardness*, John Wiley & Sons, Inc., New York, NY USA. 2009.

65 A. M. Tehrani, A. Lim and J. Brgoch, Mechanism for Unconventional Nonlinear Elasticity, *Phys. Rev. B: Condens. Matter Mater. Phys.*, 2019, **100**, 1–6.

66 J. Yang, H. Sun and C. Chen, Is Osmium Diboride An Ultra-Hard Material, *J. Am. Chem. Soc.*, 2008, **130**, 7200–7201.

67 M. Hebbache, L. Stuparević and D. Živković, A New Super-hard Material: Osmium Diboride OsB_2, *Solid State Commun.*, 2006, **139**, 227–231.